Hindawi Publishing Corporation
Journal of Nanomaterials
Volume 2015, Article ID 761517, 10 pages
http://dx.doi.org/10.1155/2015/761517

Research Article

Biocompatibility and Bioimaging Application of Carbon Nanoparticles Synthesized by Phosphorus Pentoxide Combustion Method

Shibsekhar Roy,[1] Barbara Korzeniowska,[1] Chandra K. Dixit,[2] Gowri Manickam,[3] Stephen Daniels,[3,4] and Colette McDonagh[1,3]

[1]*National Biophotonics and Imaging Platform, School of Physical Sciences, Dublin City University, Glasnevin, Dublin 9, Ireland*
[2]*National Biophotonics and Imaging Platform, School of Biotechnology, Dublin City University, Glasnevin, Dublin 9, Ireland*
[3]*Biomedical Diagnostics Institute, Dublin City University, Glasnevin, Dublin 9, Ireland*
[4]*School of Electronic Engineering, Dublin City University, Dublin 9, Ireland*

Correspondence should be addressed to Shibsekhar Roy; shibsekharroy@gmail.com

Received 1 September 2015; Revised 20 October 2015; Accepted 22 October 2015

Academic Editor: Giovanni Bongiovanni

Carbon nanoforms have emerged as a versatile bioimaging tool. In this work, we have synthesized four different carbon nanoparticles of different dimensions (10–100 nm) and variable fluorescence quantum efficiency (0.007 to 0.37) from four different carbon sources by phosphorus pentoxide-mediated combustion. The fluorescence quantum efficiency of the resulting self-passivated nanoparticles has been empirically correlated to the molecular weight and viscosity of the respective carbon source used in the synthesis. The carbon nanoparticles have been found to be significantly biocompatible as observed in the MTS assay. We have applied these biocompatible luminescent carbon nanoparticles as high brightness fluorescent probes for staining human blood platelets with very high target specificity.

1. Introduction

Fluorescent carbon nanoparticles (CNPs) or carbon nanodots (Cdots), with their reduced cytotoxicity, resistance to photobleaching, and increased biocompatibility, are of great interest as an alternative label to semiconductor quantum dots for cell imaging and other biomedical applications [1]. The origin of the fluorescence of these particles is still not clear but is thought to be related to "surface carrier traps" or in short "surface trap," which is associated with the passivating polymeric surface functional groups around a carbon core [1, 2]. The origin of the luminescence decay of CNPs is attributed to several parameters including quantum effect (i.e., the optical selection of deferentially sized nanoparticles) [3], surface group chemistry [4], surface defects and surface states [5], extent of surface passivation [1], degrees of π-conjugation [6, 7], and the electron-hole pair recombination [8]. The competition among various emission centres and traps dominate the optical properties of fluorescent CNPs. It becomes imperative to evaluate each parameter and compare various CNPs to assess the importance of these parameters leading to their luminescence properties.

The size and luminescence properties of CNP or Cdot are strongly dependent on the synthesis routes for the nanoforms. Various synthesis routes present some advantages and disadvantages to the table. The nanoforms synthesized by chemical ablation method, which is the most accessible method that can use various carbon sources, normally are highly luminescent [9–13]. However, this multistep method suffers from some shortcomings like using very harsh reaction condition, poor control of particle size-hence highly polydisperse. In comparison, the laser ablation method is very fast method that can tune surface properties [5, 14–17]. This method is poor in controlling size and the nanoforms have low quantum efficiency (QE). The electrochemical carbonization method is also a single step method which

can control size, surface of the nanostructure, and QE of the nanoform but there are very few substrates available for this method [18–21]. Other methods like solvothermal treatment [22–26] and microwave irradiation [27–29] are nontoxic, ecofriendly, and cost-effective but they cannot control the size of the nanoform.

Most CNP synthesis involves using separate carbon sources for the carbon core and for the surface passivation [30]. In this study, in order to avoid heterogeneity of the carbon core and surface, we have used a set of four single carbon sources to produce self-passivated particles in a one-step synthesis. We have chosen acetic acid as the source for the control particle (C_{ACE}) after Fang et al. [4] who used phosphorous pentoxide (P_2O_5)-mediated combustion and we compared this particle with CNPs synthesized under identical conditions using glycerol (C_{GLY}), glutaraldehyde (C_{GLU}), and polyethyleneimine (C_{PEI}). The choice of carbon precursors was dictated by the wide range of molecular weight, viscosity, and potential functionalities derived from these starting materials. The motivation for the work was 2-fold (i) to attempt to further elucidate the origin of the fluorescence on the basis of their precursors' physical properties (like molecular weight, viscosity) and (ii) to optimise the luminescence properties of the CNPs for cell imaging applications.

Use of CNPs as biolabelling agents requires an optimum combination of appreciable biocompatibility and high QE. It has earlier been observed that PEI doped CNPs with high QE displayed high cytotoxicity due to the chemical nature of ethyl imine groups exposed from the nanosurface, minimizing their scope for biological application, especially within *in vivo* experimental frame work [31]. In our CNP synthesis method, we have also included PEI to observe whether P_2O_5 hydration can nullify the functional existence of ethyl imine groups distributed on nanosurface, thus making them more suitable for *in vivo* application without compromising the luminescence properties.

2. Experimental Section

2.1. CNP Synthesis. Reagents used for the synthesis of CNP, such as acetic acid (molecular weight, MW = 60; viscosity at 20°C, η = 1.22 mPa s; density, ρ = 1.05 gm/mL), glycerol (MW = 92, η = 1200 mPa s, and ρ = 1.25 gm/mL), glutaraldehyde (MW = 100, η = 22.1 cps, and ρ = 1.06 gm/mL), and polyethyleneimine (MW = 600, η = 27000 cps, and ρ = 1.05 gm/mL), and phosphorous pentoxide were purchased from Sigma Aldrich, Ireland, and were used without further modification unless mentioned otherwise.

The reaction between 1.25 gm P_2O_5, 1 mL starting material, and 20 μL milliQ water in room temperature yielded a brown CNP solution. The samples were washed and resuspended in deionized water or physiological buffer solution for further studies depending on specific requirements.

The homogeneous solution mixture of the carbon precursor and water was carefully added to a beaker containing P_2O_5 that was kept inside a fume hood. Care was taken to avoid any possible inhalation of vapour emanating from the exothermic reaction. Here the energy required for executing the reaction is directly provided by the "self-heating" process caused by boiling of carbon precursor. Water functions as the heat reservoir as it is utilized by the carbonization reaction. The autocatalytic nature of this reaction was earlier described in detail by Fang et al. [4].

2.2. Purification. This reaction mixture was gradually cooled within 20 to 30 min. The cooled dark brown mixture of CNP was collected by water dispersion. The water dispersed CNP was purified in two stages.

(1) Centrifugation: the CNP solution was initially centrifuged for 10 min at 1000 rpm. The unreacted carbon precursor and large sized carbonaceous aggregates were discarded as pellet. The supernatant containing CNP was centrifuged for 10 min at 8000 rpm. The process was repeated for three times. The pellet containing CNP was resuspended at milliQ water for further purification.

(2) Solvent extraction: the CNP was added to water-ethyl acetate mixture and CNP extracted from both water and ethyl-acetate layer. The amount of CNP extracted from water and ethyl acetate was found to be roughly at 2 : 1 ratio for all the CNPs. This result agrees well with the observation made by Fang et al. [4].

2.3. Spectroscopy. For UV-visible spectroscopy, a Cary 50 scan UV-visible spectrophotometer (Varian) was used. For fluorescence spectroscopy, a Fluoromax spectrophotometer was used. The quantum efficiency was measured against the reference dye quinine sulphate (QS) at 10% sulphuric acid (QE = 0.55) [5]. Quinine sulphate was chosen as the reference as its emission maximum (ca. 450 nm) lies comfortably within the emission maxima range (430 to 485 nm) for various CNPs. To acknowledge this restriction for reference selection, the measured QE will be referred as relative quantum efficiency (QE_R). The QE of all CNPs were measured under conditions of 350 nm excitation and the fluorescence emission intensity was integrated in the 400 nm to 520 nm range. Samples of all the fluorophores having an absorbance value (A) between 0.01 and 0.1 (this concentration range was chosen to annul any possible quenching effect of the fluorophores) were excited at 350 nm. From the fluorescence emission spectra, the area under the emission peak (maximum wavelength of 450 nm) ranging from 400 to 520 nm was measured to calculate the integrated fluorescence (IF). The QE_R value will be calculated as follows:

$$QE_R = 0.55 \times \frac{A_{QS}}{A_{CNP}} \times \frac{IF_{CNP}}{IF_{QS}}. \quad (1)$$

2.4. Dynamic Light Scattering

2.4.1. Size Measurement. We have used the Nano-ZS (Malvern) instrument for our experiment. The instrument is equipped with a 4 mW He-Ne Laser (λ = 632 nm). The sample is poured in a 3 mL glass cuvette (path length 1 cm) with all transparent walls. Prior to the DLS study, protein samples were filtered through a 2 μm membrane filter (Acrodisc).

The operating procedure was programmed (using the DTS software supplied with the instrument) such that there are average 20 runs, each being averaged for 10 sec, and a particular R_h (hydrodynamic radius) is computed in each case and ultimately the result is presented as the distribution of R_h. In DLS one intends to measure the three-dimensional pdf (probability distribution function) for diffusion process P, a general expression is given by

$$P(r,t \mid 0,0) = (4\pi Dt)^{-3/2} \exp\left(\frac{-r^2}{4Dt}\right). \quad (2)$$

Since this function only depends on D, the diffusion constant of the system, this allows us to obtain the value for the Stokes radius $R_h = a$, if the pdf can be measured. The Stokes relation can compute the diameter of the scattering particle:

$$D = \frac{F}{6\pi\eta a}. \quad (3)$$

The link between the pdf and the power spectrum is a consequence of the translation of the relative motion of the scattering particles into phase differences of the scattered light. So if $I(t)$ is the intensity of the scattered light, then autocorrelation function $C(\tau)$ satisfies the following equation:

$$C(\tau) \sim \langle I(t)\, I(t+\tau)\rangle. \quad (4)$$

The correlation function undergoes an exponential decay with time:

$$C(\tau) \sim \exp\left(\frac{-\tau}{D}\right). \quad (5)$$

It is then straightforward to measure the diffusion coefficient D from the slope of the log C-τ plot. This (D) in turn provides the hydrodynamic size (D_h) which follows from Stokes' relation. A particular D_h is evaluated several times and the result is presented in terms of a distribution of the hydration diameter. The instrument provided the size distribution in (a) intensity mode, (b) volume mode, and (c) number mode. While the first mode, providing the size distribution of scattered intensity, is more sensitive to alteration in D_h (intensity varying as $\sim {D_h}^6$), the second and third mode provide size distribution of volume and number of particles, respectively, in the light path. For monitoring the population of aggregates (whose numbers are appreciably high in some cases) the multimode intensity distribution was used.

2.4.2. Zeta Potential Measurement by Laser Doppler Velocimetry. The same instrument Zetasizer nano calculates the zeta potential. In an ionic solution, the development of a net charge on the surface of a particle alters the ionic distribution in the interfacial region that results in the increase in counter ion concentration close to the surface. Thus, an electrical double layer exists surrounding each particle. The inner part of the layer, that is, the Stern layer, is characterized by strongly bound ions and the outer layer consists of loosely bound diffusing ions. Within this diffusive layer, the ions as well as particles form a stable entity confined by a boundary. With the gravity induced particle movement, ions within that boundary also move along it but not the ions beyond this boundary. The potential existing in this boundary is called the zeta potential.

This is to be remembered that zeta potential is purely an electrokinetic property of the electrical double layer surrounding the subject but not the surface of the subject itself. This quantity is measured by determining the electrophoretic mobility and then applying the value in Henry's equation. The velocity of a particle in an electric field is known as electrophoretic mobility (U_E). Now, applying this value to Henry's equation we will obtain the value of zeta potential (z):

$$z = \frac{3\eta U_E}{2\varepsilon \cdot f(K_a)}, \quad (6)$$

where η is viscosity; ε is dielectric constant; $f(K_a)$ is Henry's function.

A special capillary cell is used for this measurement with embedded electrodes at either of the two ends. Particles move towards the electrode of the opposite charge and their velocity is measured and expressed in unit field strength as their mobility.

Now, the technique that is used for this measurement is Laser Doppler Velocimetry. This technique efficiently measures the velocity of tiny particles within the fluid streams moving at the velocity of the fluid. The receiving optics is focused to relay the scattering particles in the cell. After being scattered at an angle of 17°, the beam is combined with the scattered beam and produces a fluctuating signal, whose fluctuation rate is proportional to the particle velocity. Then a signal processor extracts the characteristic frequency of the scattered light.

2.5. Cellular Experiments. Dulbecco's Modified Eagles Medium (DMEM) was purchased from Sigma Aldrich, Ireland. Fetal bovine serum (FBS) and Penicillin-Streptomycin were obtained from GIBCO, Ireland. T-75 flasks and 96-well plates were acquired from Fisher Scientific, UK, and Nunc, USA, respectively. CellTiter 96 Aqueous One Solution Reagent was purchased from Promega, Ireland. Aqueous carbon nanoparticles (10 μg/mL) solutions were prepared using sterile deionized MilliQ water. All chemicals were of analytical grade and were used without further purification.

2.6. Cell Culture. Human Osteosarcoma Epithelial (U_2OS) cells were grown in DMEM supplemented with 10% v/v FBS and 1% v/v Penicillin-Streptomycin. Cells were cultured in T-75 flasks at 37°C, 5% CO_2, with maintaining the cell confluency between 80% and 90% and low cell passage number (below 40).

2.7. Cytotoxicity Studies. Cytotoxicity of carbon nanoparticles was evaluated using a colorimetric cell proliferation assay. U_2OS cells were plated in a 96-well plate at the concentration of 2.5×10^3 cells/well and left in the incubator for 4 h to allow cells adhere to the well. Then carbon nanoparticles at different final concentration (50 μg/mL, 100 μg/mL, and 150 μg/mL) were added to the media. The total time of exposure of

cells to nanoparticles was 72 h. The negative control was also prepared with cells incubated in DMEM not containing the carbon nanoparticles. At the end the cell proliferation assay was performed according to the manufacture's protocol. The media containing carbon nanoparticles were aspirated from wells and fresh media (100 μL) with the colorimetric reagent (MTS) (20 μL) were added to wells. The absorbance was detected at 490 nm for each well after 1 h with a Safire II microplate reader (Tecan System Inc., Austria). In order to calculate the cell viability the absorbance values obtained for samples exposed to the nanomaterial at 3 different concentrations were compared to the negative control using a standard one-way analysis of variance (ANOVA, mean (n = 3), ±SD, three independent experiments).

2.8. Instrument Details. For UV-visible spectroscopy, a Cary 50 scan UV-visible spectrophotometer (Varian) was used. For fluorescence spectroscopy, a Fluoromax spectrophotometer was used. The QE of all CNPs were measured under conditions of 350 nm excitation and the fluorescence emission intensity was integrated in the 400 nm to 520 nm range.

Fluorescence lifetimes were measured by a TCSPC instrument. The details are as follows:

System: FluoTime100, PicoQuant.

Laser line: 375 nm, 450 nm, PicoQuant.

Pulse generator: Thurlby Thandar Instruments.

Detector: SPAD, PicoQuant.

Filters: not required as beam path is right angles.

Software: TimeHarp or PicoHarp, PicoQuant.

For the TEM measurement, a Hitachi 7000 transmission electron microscope was operated at 100 kV. Image capture was performed digitally by a Megaview 2 CCD camera. Specimens were prepared by putting a drop of the ethanolic solutions of the nanoparticles on a Formvar carbon-coated copper grid (Agar Scientific).

Raman spectra were obtained with a Jobin-Yvon LabRam HR800 Raman microscope. An Ar ion laser of 488 nm wavelength was used as the excitation source. A grating of 2400 grooves/nm was employed. The accumulation time was 10 seconds and 3 accumulations were averaged for each spectrum.

2.9. Platelet Capture on Glass Slides. Poly-L-lysine (PLL) slides (Sigma Aldrich, Ireland) were washed with methanol and N_2 dried. Glutaraldehyde (Sigma Aldrich, Ireland) was prepared at 10% (v/v) solution in deionized water (DIW). The PLL slides were incubated with 10% glutaraldehyde solution for 20 min followed by thorough washing with DIW.

Whole blood was obtained from consenting healthy donors. Platelet-rich plasma (PRP) was obtained by mild centrifugation of whole blood at 1200 rpm. The supernatant serum was stored while discarding the cellular pellet. PRP was reconstituted by adding 1 mL of 1 mM PBS (Thermo Fischer, Ireland) to 1 mL of PRP and was stored at 4 degrees centigrade for further use. Regulatory biosafety measures were taken in compliance with the bioethics rules (CREC, DCU) during the haematological experiments.

Prior to platelet capture on the activated slide, fibrinogen (Sigma Aldrich, Ireland) was spotted on the activated PLL slide at a spot size of 10 μL for 15 min followed by washing with 1 mM PBS and drying with N_2. Later, the slide was blocked with 3% (w/v) BSA (Sigma Aldrich, Ireland) and was incubated for 30 min followed by thorough washing with 1 mM PBS. PRP was incubated exactly over the fibrinogen spot and incubated for 15 min followed by washing.

2.10. CNP-Antibody Conjugation. First, the CNP samples (10 μg/mL) were treated with aminopropyl triethoxysilane (2% APTES in ethanol for three hours) for amine-silanization of the nanosurface. Animated CNPs were washed 3 times in ethanol and then resuspended in DIW. Amine silanized CNP samples were first treated with glutaraldehyde (10%) for 30 min followed by washing with DIW 2x and with ethanol 2x. The particles were N_2 dried and resuspended in 1 mM PBS prior to antibody conjugation. Anti-CD41 antibody (10 μg/mL) in 1 mM PBS was then conjugated to the glutaraldehyde-activated CNP (10 μg/mL) and incubated for 20 min followed by extensive PBS washing. The control CNPs (CNP with anti-IgG) were also treated identically.

2.11. Fluorescence Microscopy. To achieve efficient platelet probing (as a part of the haematological diagnostic initiative of the NBIPI project) we have chosen the platelet surface receptor CD41 as our platelet probing target. Anti-CD41 conjugated CNP samples were spotted exactly over the platelet spot and incubated for 15 min followed by washing with PBS with appropriate controls. Imaging was performed using fluorescence microscopy (Hamamatsu) using FITC filter at an objective of 10x. For image analysis experiment, the fluorescence images were obtained in grey scale as binary image. The settings were kept the same throughout the experiment. The MATLAB script for the image analysis is provided in the ESI.

3. Result and Discussion

3.1. Spectroscopy. To evaluate the primary photophysical properties of the CNPs, UV-Vis and fluorescence spectroscopy studies were carried out. The absorption spectra for the synthesized CNPs have been shown in Figure 1(a). The spectra show the usual broad peak at ca. 350 nm for all the CNPs. A secondary absorption "shoulder" was also observed at ca. 450 nm for C_{GLU} and C_{PEI}. This secondary shoulder may be attributed to the complex or aggregated structure for these CNPs. When the CNPs were excited at 350 nm, the emission spectra were observed and were shown in Figure 1(b). The emission maxima for C_{GLU} and C_{PEI} were observed at 430 nm while that for C_{ACE} and C_{GLY} is at 485 nm.

To further evaluate the emissive properties of these CNPs, their relative quantum efficiency (QE_R) was measured by the method already described in the experimental section. The QE_R trend has been demonstrated in Table 1. The values are highly diverse where QE_R of C_{ACE} and C_{GLY} is <0.01 and QE_R for C_{GLU} and C_{PEI} are 0.14 and 0.37. The origin

Table 1: Fluorescence properties for the CNPs.

CNPs	Average lifetime τ_{av} (ns)	Relative quantum efficiency QE_R	Radiative decay constant Γ (μs^{-1})	Nonradiative decay constant K_{nr} (ns^{-1})
C_{ACE}	3.84	.0074 ± .0003	1.9	.2585
C_{GLY}	4.49	.0087 ± .00035	1.9	.2208
C_{GLU}	1.50	.1353 ± .0286	90.0	.5767
C_{PEI}	6.65	.3708 ± .019	55.8	.0946

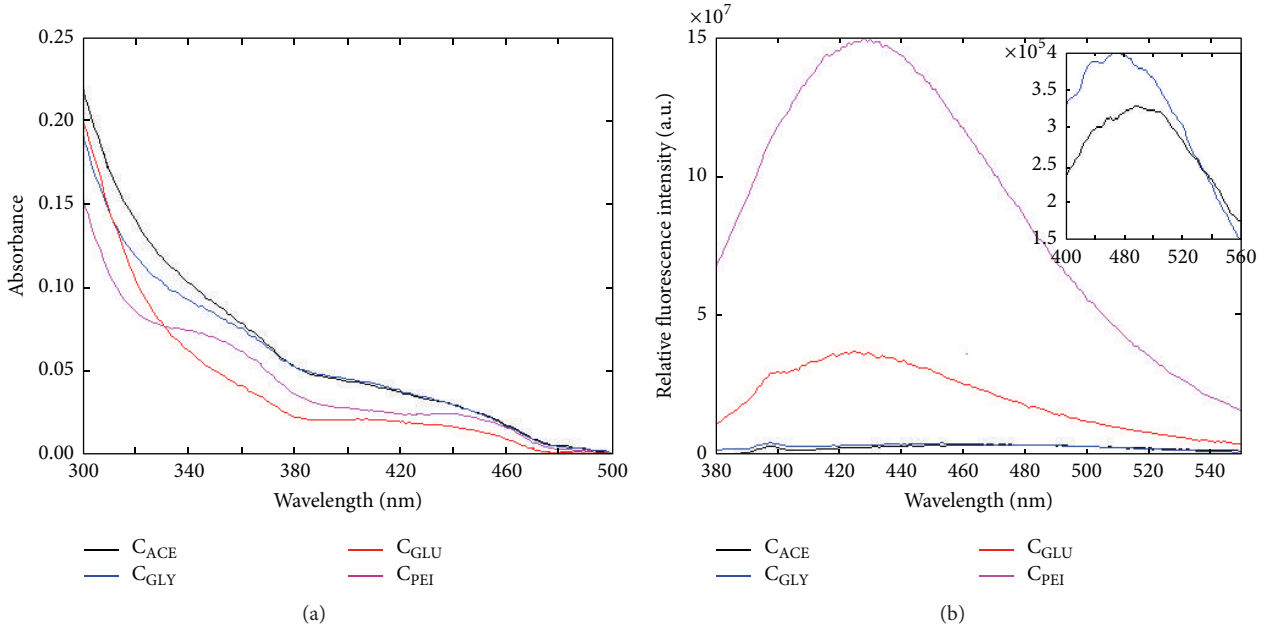

Figure 1: (a) UV/Vis spectra of CNPs are described. (b) Fluorescence emission spectra of CNPs (keeping the absorbance ca. 0.1 for all the CNPs at 350 nm) when excited at 350 nm. The inset magnifies the fluorescence emission spectra of C_{ACE} and C_{GLY}.

of this luminescence property is attributed to the surface traps created due to the self-passivation of the nanosurface. However the huge variation is observed mainly due to the physicochemical nature of the carbon precursors and the size of the nanoparticles. This part will be discussed in detail in the later section.

So high-QE_R CNPs have potential application as luminescent cellular probes. On the other hand, the low-QE_R CNPs have potential application as biomolecule binder stains as the spectral range of these CNPs are similar to the popular commercial dyes like Hoechst-33342 (cell permeable nucleic acid counter stain having excitation wavelength 343 nm and emission wavelength 483 nm) and DAPI (strong DNA binding stain having excitation wavelength 345 nm and emission wavelength 455 nm). However, a detailed photophysical evaluation of these low-QE_R CNPs as biomolecule-specific luminophore is beyond the scope of this paper. The plot for absorption versus integrated fluorescence for QE_R measurement can be found in the ESI (Supporting Figure S1; see Supplementary Material available online at http://dx.doi.org/10.1155/2015/761517).

Table 1 also shows the fluorescence lifetime (τ) for the CNPs. The lifetime and associated fluorescence decay parameters were measured using total counting single photon decay (TCSPC). The detailed fluorescence decay plots can be found in the ESI (Supporting Figure S2) The radiative (Γ) and nonradiative (K_{nr}) decay constants were calculated from QE_R and τ data according to the related reference [6]. It is to be noted that Γ and K_{nr} are very high for C_{GLU} while K_{nr} is very low for C_{PEI} which has the highest QE. They high degree of variability in the fluorescence property of the CNPs will be discussed in the light of their carbon sources.

3.2. Size and Stability

3.2.1. HRTEM Study. The size distribution of the CNPs under TEM showed moderate-to-high monodispersity as evinced by the TEM images in Figure 2. For the control particle, C_{ACE}, the HRTEM images are shown in Figure 2(a) which show the presence of nanoparticles with the average size of 19 nm (statistical size distribution is included in Table 2) that is similar to the result observed by Fang et al. [4]. Similar size (mean size 16 nm) was observed for C_{GLY} as observed in Figure 2(b). The mean sizes for the other CNPs were observed to be larger than 35 nm as Figures 2(c) and 2(d) showed the mean sizes of C_{GLU} and C_{PEI} to be 39 and 36 nm, respectively.

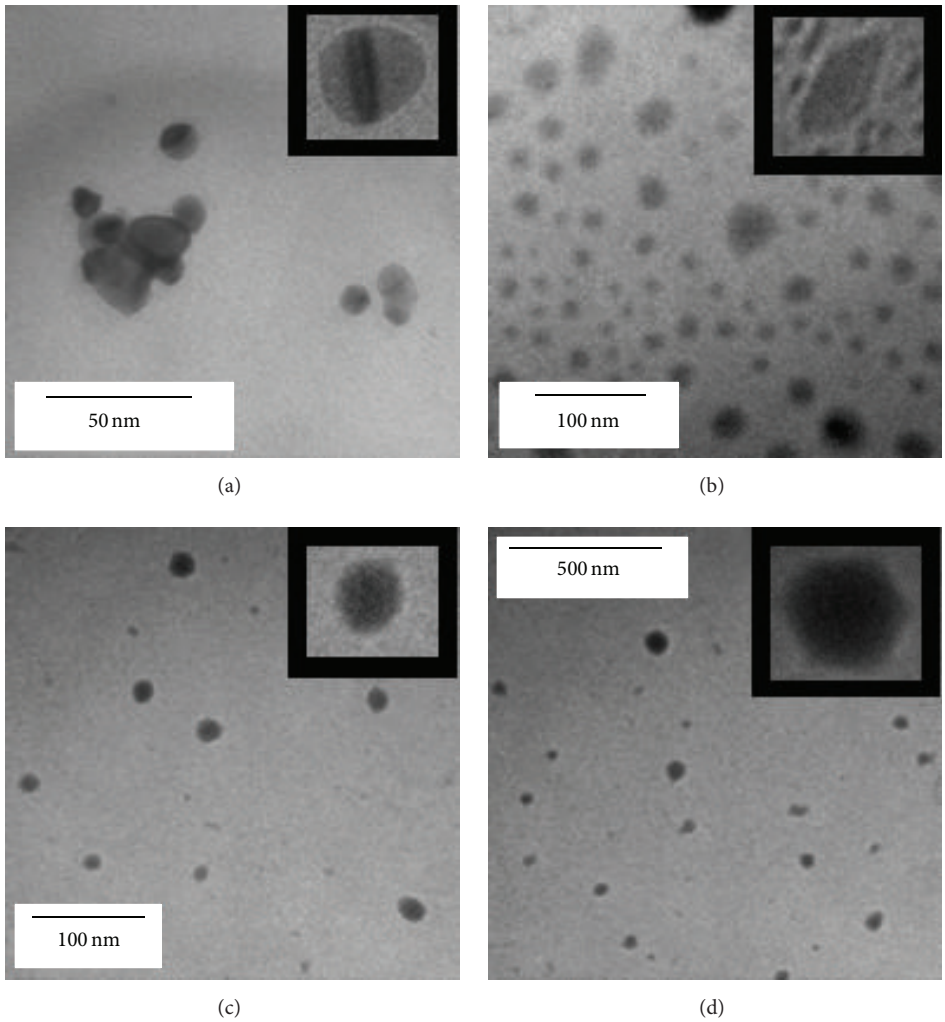

Figure 2: HRTEM images for (a) C_{ACE}, (b) C_{GLY}, (c) C_{GLU}, and (d) C_{PEI} are shown.

Table 2: Table comparing the size distribution obtained in TEM and DLS, PDI values, and zeta potential values obtained from the DLS instrument.

Sample	TEM	DLS		
	Size (nm)	Size by number (nm)	PDI	Zeta potential (mV)
C_{ACE}	19.6 ± 3.3	30.3 ± 6.1	0.25	−20.5
C_{GLY}	16.3 ± 2.1	25.6 ± 10.2	0.17	−26.2
C_{GLU}	38.9 ± 9.6	45.4 ± 4.1	0.09	−34.3
C_{PEI}	36.4 ± 6.3	65.6 ± 10.7	0.12	−31.8

3.2.2. DLS Study. The hydrodynamic diameter of CNPs was found to agree well with that of the TEM diameter as Table 2 shows that the value of hydrodynamic diameters is slightly larger than that of the TEM ones for the presence of water layer outside the CNPs. However, for C_{PEI} the hydrodynamic size is close to double of the TEM one which is possibly due to some degree of oligomerization for the CNP. The zeta potential values, as displayed in Table 2 as well, are ranged from −20.5 mV (C_{ACE}) to −34.3 mV (C_{GLU}). This indicates moderate-to-high level of hydrodynamic stability, which is required for high performance bioprobes.

3.2.3. Correlating the Parameters Determining Luminescence. To identify the correlation between the fluorescence property of the CNPs with their hydrodynamic sizes (D_h) as well as the molecular weight (MW) of their corresponding carbon sources, an empirical correlogram was constructed. It is worth mentioning here that we have considered hydrodynamic sizes instead of the TEM diameters because the luminescence measurements were performed in the aqueous environment. The correlogram, as described in Figure 3, is a three-dimensional plot of QE_R values as function of MW and D_h. The plot shows a steady nonlinear increment of QE_R with respect to MW and D_h. However, the very high value of QE_R for C_{PEI} demands special attention. The photoluminescence mechanism for PEI doped Cdots was earlier hypothesized by Yang's group as Crosslink Enhanced Emission (CEE) effect

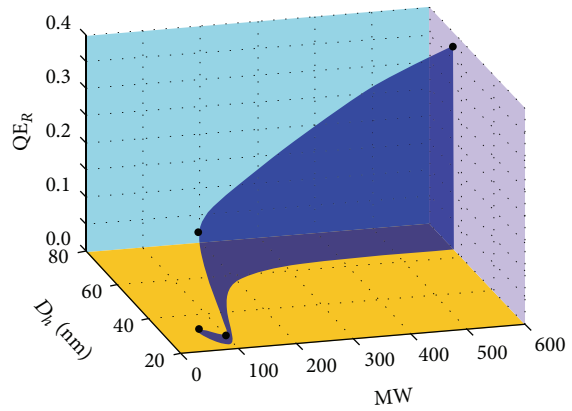

FIGURE 3: 3-dimensional plot of quantum efficiency of the CNPs as the function of their hydrodynamic size (D_h) and precursors' molecular weight.

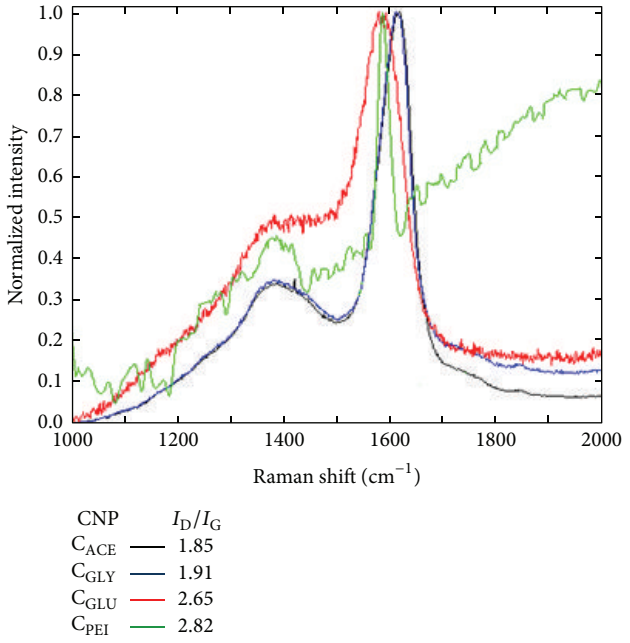

FIGURE 4: Raman signatures for all the CNPs. Along with their I_D/I_G values.

[27]. The abundance of secondary and tertiary amine leads to a highly crosslinked carbon framework. This crosslinked carbon mesh works as a sink for rotational and vibrational degrees of freedom to significantly decrease the nonradiative decay process and hence significantly decrease the value of K_{nr} as shown in Table 1.

3.3. Raman Spectroscopy. The electronic basis behind emergence of CNP luminescence was further explored by Raman spectroscopy. Figure 4 shows the description of the Raman active features of the CNPs. The result shows the relative intensity of the sp^3 carbon rich disordered D peak at ca. 1385 cm^{-1} and the E_{2g} mode of sp^2 carbon rich graphite/graphene G peak at ca. 1585 cm^{-1}. The ratio (r) of the intensity of the sp^3 carbon rich disordered D peak at ca. 1385 cm^{-1} and the sp^2 carbon rich graphite/graphene G peak at ca. 1585 cm^{-1} for

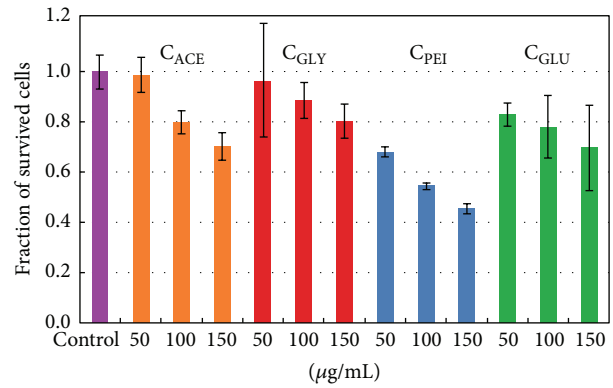

FIGURE 5: The MTS assay result for CNPs is described as bar diagram.

the CNPs is seen to be similar for C_{ACE} and C_{GLY} but increases for C_{GLU} and C_{PEI}. The ratio of D-peak area and G-peak area denotes the structural purity of the graphitic material. This (I_D/I_G) ratio increase is indicative of the increased amorphous nature of these surfaces whereby the evolution of the cubic structure leads to pressure induced breakdown of sp^2 bonds with concomitant generation of sp^3 bonds [31]. This orbital reorganisation is possibly playing a key role in creating new band structures and thus a much higher value of radiative decay constant is observed for C_{GLU} and C_{PEI} in Table 1 compared to C_{ACE} and C_{GLY}. Similar results were reported when the chemical nature of autocatalytically formed CNP surface was earlier described by Fang et al. [4], who proposed crystalline graphitic nature for these CNPs.

The anomalous behaviour of the I_D/I_G peak ratio from different CNPs can be explained by some critical observation made by Stankovich et al. [32]. They have demonstrated that the relative intensity of the D-peak with respect to the G-peak depends on the degree of oxidation taking place on the graphene oxide surface. For C_{GLU} and C_{PEI} there are significant abundance of surface traps on the carbon nanosurface to accommodate larger concentration of oxygen molecules when compared to C_{ACE} and C_{GLY}. The reason is attributed to higher molecular weight of carbon precursors for C_{GLU} and C_{PEI} leading to more complex carbon crosslinking structures with abundant energy traps favouring oxidation. This hypothesis is also supported by the result of Yang's group who proposed Crosslink Enhanced Emission (CEE) effect to explain enhanced luminescence properties for CNPs prepared from PEI carbon precursor [4].

3.4. Cell Toxicity Studies. Before evaluating the efficiency of the CNPs as fluorescent labels, it is imperative to assess whether they have significant cytotoxic effect on cells. To evaluate the potential toxicity of the nanoparticles within a cell, an MTS assay was used to measure cell proliferation in the U_2OS cell lines following exposure to different concentrations to as high as 1 mg/mL of nanoparticles for 72 h.

The results obtained from these studies, presented in Figure 5, were subjected to one-way ANOVA statistical analysis and the analyses. There was significant effect of the concentration of CNP on the cell viability for C_{ACE} and C_{PEI}

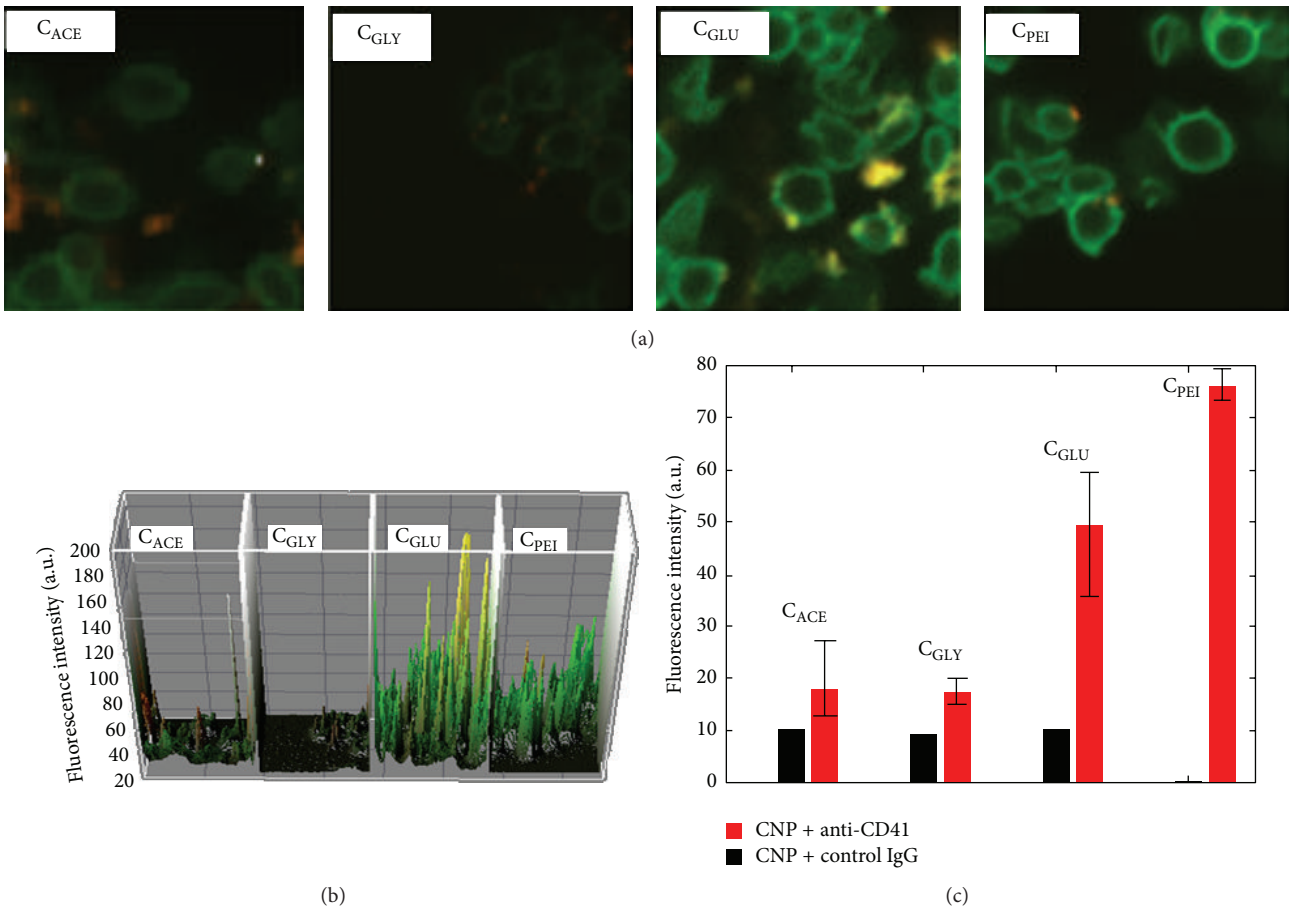

FIGURE 6: (a) Fluorescence microscopy image of human blood platelet by anti-CD41 conjugated CNPs. (b) Fluorescence intensity (z-axis) analysis showed the relative intensity distributions for the fluorescence images of (a). (c) Image analysis result of platelet staining for all CNPs with the red bar corresponding to anti-CD41 conjugation and black bar corresponding to the control IgG. The raw grey image data is shown in Figure S3 of Supporting Information.

at the level of $p < 0.02$. The statistical analysis has now been included in the ESI as Figure S4 and Table S1. Within the CNPs, C_{PEI} showed the lowest value of LD_{50} (i.e., the lethal concentration required to cause 50% cell death) which is more than 50 μg/mL. This value is significantly higher than the earlier reported LD_{50} value of 3.125 μg/mL for a PEI modified magnetic nanoparticle after 72 h incubation [33], which essentially made our system nontoxic as the fluorescence bioassays for this paper were performed at 10 μg/mL concentration. These results indicate good biocompatibility of the nanoparticles, which is crucial to intracellular sensing applications.

3.5. Fluorescence Staining. The potential of the CNPs as fluorescent labels for cell staining was demonstrated by conjugating all nanoparticles with the blood platelet external surface-specific antibody, anti-CD41, and carrying out a staining experiment. The surface functionalization of CNP nanosurface by APTES and then by anti-CD41 antibody was monitored electrostatically by observing their zeta potential trend through the functionalization steps (detailed profile of zeta potential monitoring is available in ESI as Table S2). Platelets were stabilised on a fibrinogen coated glass surface using glutaraldehyde and they were targeted by anti-CD41 conjugated CNPs taking the anti-IgG conjugated CNP as the control. The slides were analysed using fluorescence microscopy. Figure 6(a) shows the fluorescence response for platelet probing by anti-CD41 conjugated CNPs. To assess nonspecific binding, IgG conjugated CNPs were also tested against platelets. It is clear that the intensity profile correlates well with the QE results whereby C_{ACE} and C_{GLY} are similar, whereas C_{GLU} and C_{PEI} show significantly higher fluorescence response. The z-axis analysis of fluorescence intensity for the corresponding CNP-tagged platelet samples is provided in Figure 6(b). Furthermore, probing specificity and fluorescence probing intensity by CNPs were quantitatively measured by analysing fluorescence images using MATLAB image analysis toolbox (MATLAB script is available in the ESI). To achieve this, the fluorescence image was captured under grey scale (all the grey scale images may be found in the ESI as Figure S3). The ratio between white and black pixels within the grey scale images (averaged over three slides) for CNPs was demonstrated as a bar diagram in Figure 6(c). The bar diagram clearly showed that C_{GLU} and C_{PEI} are the most

fluorescent probing agents compared to the other CNPs. In addition, the significant decrease in nonspecific binding for the C_{PEI} was also observed to strengthen the potential of C_{PEI} as an efficient bioprobe.

4. Conclusion

In conclusion, self-passivated CNPs have been synthesized from four different single carbon sources and their photophysical properties and surface morphology have been investigated. The high QE of C_{GLU} and C_{PEI} was correlated with the increased amorphous nature of the surface and the presence of the cubic phase of graphite. The improved optical properties may also be related to the higher polymeric nature of the precursors. These particles are easy to synthesize and functionalize and are good candidates for use as high brightness probes as shown by a model cell staining experiment.

Conflict of Interests

The authors declare that there is no conflict of interests regarding the publication ofthis paper.

Acknowledgments

This work was supported through the National Biophotonics and Imaging Platform, Ireland, and funded by the Irish Government's Programme for Research in Third Level Institutions, Cycle 4, National Development Plan 2007–2013.

References

[1] S. N. Baker and G. A. Baker, "Luminescent carbon nanodots: emergent nanolights," *Angewandte Chemie—International Edition*, vol. 49, no. 38, pp. 6726–6744, 2010.

[2] Y.-P. Sun, B. Zhou, Y. Lin et al., "Quantum-sized carbon dots for bright and colorful photoluminescence," *Journal of the American Chemical Society*, vol. 128, no. 24, pp. 7756–7757, 2006.

[3] H. Li, X. He, Z. Kang et al., "Water-soluble fluorescent carbon quantum dots and photocatalyst design," *Angewandte Chemie—International Edition*, vol. 49, no. 26, pp. 4430–4434, 2010.

[4] Y. Fang, S. Guo, D. Li et al., "Easy synthesis and imaging applications of cross-linked green fluorescent hollow carbon nanoparticles," *ACS Nano*, vol. 6, no. 1, pp. 400–409, 2012.

[5] S.-L. Hu, K.-Y. Niu, J. Sun, J. Yang, N.-Q. Zhao, and X.-W. Du, "One-step synthesis of fluorescent carbon nanoparticles by laser irradiation," *Journal of Materials Chemistry*, vol. 19, no. 4, pp. 484–488, 2009.

[6] X.-J. Mao, H.-Z. Zheng, Y.-J. Long et al., "Study on the fluorescence characteristics of carbon dots," *Spectrochimica Acta Part A: Molecular and Biomolecular Spectroscopy*, vol. 75, no. 2, pp. 553–557, 2010.

[7] A. B. Bourlinos, R. Zbořil, J. Petr, A. Bakandritsos, M. Krysmann, and E. P. Giannelis, "Luminescent surface quaternized carbon dots," *Chemistry of Materials*, vol. 24, no. 1, pp. 6–8, 2012.

[8] S. Srivastava and N. S. Gajbhiye, "Carbogenic nanodots: photoluminescence and room-temperature ferromagnetism," *ChemPhysChem*, vol. 12, no. 14, pp. 2624–2632, 2011.

[9] S. C. Ray, A. Saha, N. R. Jana, and R. Sarkar, "Fluorescent carbon nanoparticles: synthesis, characterization, and bioimaging application," *The Journal of Physical Chemistry C*, vol. 113, no. 43, pp. 18546–18551, 2009.

[10] L. Han, D. Ghosh, W. Chen, S. Pradhan, X. Chang, and S. Chen, "Nanosized carbon particles from natural gas soot," *Chemistry of Materials*, vol. 21, no. 13, pp. 2803–2809, 2009.

[11] Z.-A. Qiao, Y. Wang, Y. Gao et al., "Commercially activated carbon as the source for producing multicolor photoluminescent carbon dots by chemical oxidation," *Chemical Communications*, vol. 46, no. 46, pp. 8812–8814, 2010.

[12] Y. Dong, N. Zhou, X. Lin, J. Lin, Y. Chi, and G. Chen, "Extraction of electrochemiluminescent oxidized carbon quantum dots from activated carbon," *Chemistry of Materials*, vol. 22, no. 21, pp. 5895–5899, 2010.

[13] H. Peng and J. Travas-Sejdic, "Simple aqueous solution route to luminescent carbogenic dots from carbohydrates," *Chemistry of Materials*, vol. 21, no. 23, pp. 5563–5565, 2009.

[14] X. Li, H. Wang, Y. Shimizu, A. Pyatenko, K. Kawaguchi, and N. Koshizaki, "Preparation of carbon quantum dots with tunable photoluminescence by rapid laser passivation in ordinary organic solvents," *Chemical Communications*, vol. 47, no. 3, pp. 932–934, 2011.

[15] L. Cao, X. Wang, M. J. Meziani et al., "Carbon dots for multiphoton bioimaging," *Journal of the American Chemical Society*, vol. 129, no. 37, pp. 11318–11319, 2007.

[16] S.-T. Yang, L. Cao, P. G. Luo et al., "Carbon dots for optical imaging in vivo," *Journal of the American Chemical Society*, vol. 131, no. 32, pp. 11308–11309, 2009.

[17] S.-T. Yang, X. Wang, H. Wang et al., "Carbon dots as nontoxic and high-performance fluorescence imaging agents," *The Journal of Physical Chemistry C*, vol. 113, no. 42, pp. 18110–18114, 2009.

[18] J. Zhou, C. Booker, R. Li et al., "An electrochemical avenue to blue luminescent nanocrystals from multiwalled carbon nanotubes (MWCNTs)," *Journal of the American Chemical Society*, vol. 129, no. 4, pp. 744–745, 2007.

[19] D. B. Shinde and V. K. Pillai, "Electrochemical preparation of luminescent graphene quantum dots from multiwalled carbon nanotubes," *Chemistry—A European Journal*, vol. 18, no. 39, pp. 12522–12528, 2012.

[20] L. Bao, Z.-L. Zhang, Z.-Q. Tian et al., "Electrochemical tuning of luminescent carbon nanodots: from preparation to luminescence mechanism," *Advanced Materials*, vol. 23, no. 48, pp. 5801–5806, 2011.

[21] L. Zheng, Y. Chi, Y. Dong, J. Lin, and B. Wang, "Electrochemiluminescence of water-soluble carbon nanocrystals released electrochemically from graphite," *Journal of the American Chemical Society*, vol. 131, no. 13, pp. 4564–4565, 2009.

[22] Z.-C. Yang, M. Wang, A. M. Yong et al., "Intrinsically fluorescent carbon dots with tunable emission derived from hydrothermal treatment of glucose in the presence of monopotassium phosphate," *Chemical Communications*, vol. 47, no. 42, pp. 11615–11617, 2011.

[23] S. Zhu, Q. Meng, L. Wang et al., "Ultrafast synthesis of nitrogen-doped carbon dots via neutralization heat for bioimaging and sensing applications," *Angewandte Chemie International Edition*, vol. 125, pp. 4045–4049, 2013.

[24] Y. Yang, J. Cui, M. Zheng et al., "One-step synthesis of amino-functionalized fluorescent carbon nanoparticles by hydrothermal carbonization of chitosan," *Chemical Communications*, vol. 48, no. 3, pp. 380–382, 2012.

[25] B. De and N. Karak, "A green and facile approach for the synthesis of water soluble fluorescent carbon dots from banana juice," *RSC Advances*, vol. 3, no. 22, pp. 8286–8290, 2013.

[26] Z. Zhang, J. Hao, J. Zhang, B. Zhang, and J. Tang, "Protein as the source for synthesizing fluorescent carbon dots by a one-pot hydrothermal route," *RSC Advances*, vol. 2, no. 23, pp. 8599–8601, 2012.

[27] H. Zhu, X. Wang, Y. Li, Z. Wang, F. Yang, and X. Yang, "Microwave synthesis of fluorescent carbon nanoparticles with electrochemiluminescence properties," *Chemical Communications*, pp. 5118–5120, 2009.

[28] X. Zhai, P. Zhang, C. Liu et al., "Highly luminescent carbon nanodots by microwave-assisted pyrolysis," *Chemical Communications*, vol. 48, no. 64, pp. 7955–7957, 2012.

[29] Y. Liu, N. Xiao, N. Gong et al., "One-step microwave-assisted polyol synthesis of green luminescent carbon dots as optical nanoprobes," *Carbon*, vol. 68, pp. 258–264, 2014.

[30] F. Wang, Z. Xie, H. Zhang, C.-Y. Liu, and Y.-G. Zhang, "Highly luminescent organosilane-functionalized carbon dots," *Advanced Functional Materials*, vol. 21, no. 6, pp. 1027–1031, 2011.

[31] S. Zhu, L. Wang, N. Zhou et al., "The crosslink enhanced emission (CEE) in non-conjugated polymer dots: from the photoluminescence mechanism to the cellular uptake mechanism and internalization," *Chemical Communications*, vol. 50, no. 89, pp. 13845–13848, 2014.

[32] S. Stankovich, D. A. Dikin, R. D. Piner et al., "Synthesis of graphene-based nanosheets via chemical reduction of exfoliated graphite oxide," *Carbon*, vol. 45, no. 7, pp. 1558–1565, 2007.

[33] C. Hoskins, L. Wang, W. P. Cheng, and A. Cuschieri, "Dilemmas in the reliable estimation of the in-vitro cell viability in magnetic nanoparticle engineering: which tests and what protocols?" *Nanoscale Research Letters*, vol. 7, article 77, 22 pages, 2012.